



Hydraulic conductivity and self-healing performance of Engineered Cementitious Composites exposed to Acid Mine Drainage

Hao-Liang Wu^{a,b,c}, Yan-Jun Du^{a,*}, Jing Yu^b, Yu-Ling Yang^a, Victor C. Li^c

^a Jiangsu Key Laboratory of Urban Underground Engineering & Environmental Safety, Institute of Geotechnical Engineering, Southeast University, Nanjing 210096, China

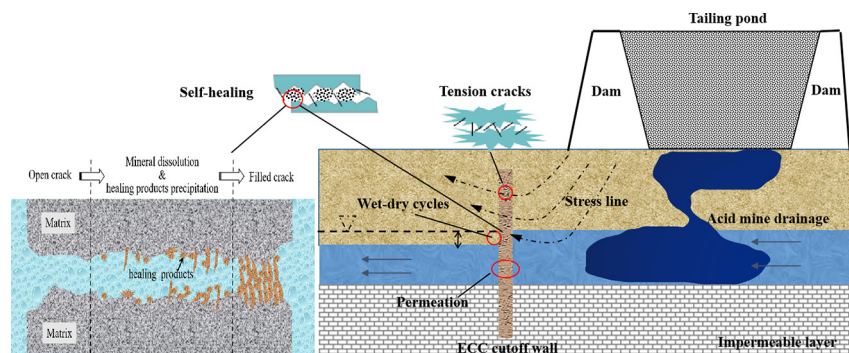
^b Department of Civil and Environmental Engineering, Hong Kong University of Science and Technology, Hong Kong SAR, China

^c Department of Civil and Environmental Engineering, University of Michigan, Ann Arbor, MI 48105, USA

HIGHLIGHTS

- MgO addition considerably improves self-healing and reduces permeability of ECC.
- Permeability of pre-strained ECC specimens is up to 1.32% and below 1×10^{-8} m/s.
- Permeability of MgO-ECC is 57.84% and 49.8% lower than ECC in tap water and AMD.
- RF drops 64% and 52% for the ECC and MgO-ECC as tensile strain increases to 2%.
- MgO additive yields formation of hydromagnesite and brucite as self-healing products.

GRAPHICAL ABSTRACT



ARTICLE INFO

Article history:

Received 14 November 2019

Received in revised form 1 February 2020

Accepted 2 February 2020

Available online 04 February 2020

Editor: Christian Herrera

Keywords:

Engineered cementitious composite

Hydraulic conductivity

Self-healing

Acid mining drainage

Reactive MgO

ABSTRACT

Engineered Cementitious Composite (ECC) is proposed as a promising vertical cutoff wall material to contain acid mine drainage (AMD). The study presents comprehensive investigations of hydraulic conductivity of ECC permeated with AMD and self-healing of ECC subjected to wet-dry cycles. The effectiveness of incorporating reactive magnesia (MgO) into ECC for self-healing enhancement is also investigated. The chemical species formed in ECC and MgO-ECC specimens after exposure to AMD are investigated via SEM, FTIR, XRD and TGA analyses. The results show hydraulic conductivity of un-cracked and cracked ECC and MgO-ECC specimens pre-strained up to 1.32% is below commonly accepted limits of 10^{-8} m/s when permeated with AMD. The self-healing capacity of ECC specimens subjected to wet-dry cycles using both tap water and AMD as immersing liquids is improved by MgO addition. MgO addition is also beneficial for reducing hydraulic conductivity of un-cracked and cracked ECC specimens permeated with AMD. MgO addition results formation of new self-healing products including hydromagnesite and brucite when exposed to tap water, and hydrotalcite-like phase (Ht) when exposed to AMD.

© 2020 Elsevier B.V. All rights reserved.

1. Introduction

Acid mine drainage (AMD) is produced when minerals such as pyrite (FeS_2), pyrrhotite (Fe_{1-x}S), chalcocopyrite (CuFeS_2) and marcasite (FeS_2) are exposed to oxygen and water (Valente and Gomes, 2009). AMD contains hydrogen ions (H^+), heavy metals (i.e., Fe, Zn, Pb, Cu,

* Corresponding author.

E-mail address: duyanjun@seu.edu.cn (Y.-J. Du).

Ni) and sulfate ions which pose potential threats to humans, plants and aquatic organisms (Valente and Gomes, 2009; Espana et al., 2005). Thus, AMD containment or treatment actions represent urgent developments for addressing social, environmental and economic concerns (Kashir and Yanful, 2000; Edraki et al., 2014). The major engineered barriers for controlling AMD seepage from tailings disposal facility are geosynthetic clay liners (GCLs), compacted soil liners, and vertical cutoff walls (Kashir and Yanful, 2000; USEPA, 1994; Fall et al., 2009). As a cost-effective pollution-controlled method, vertical cutoff walls have been successfully applied to manage contaminant flow in the vicinity of tailing dams (Kashir and Yanful, 2000; Fall et al., 2009). Depending on the backfill materials, vertical cutoff walls can be classified as soil-bentonite (SB), cement-bentonite or slag-cement-bentonite (CB) and soil-cement-bentonite (SCB), which have been implemented in lab-scale research and contaminated site remediation projects (Yang et al., 2018; Ruffing and Evans, 2014; Wu et al., 2019a). The US Environmental Protection Agency (EPA) suggests a hydraulic conductivity less than 10^{-8} for SB walls and 10^{-9} m/s for CB and SCB walls (USEPA, 1994; Joshi et al., 2009).

Recently, a family of high performance fiber-reinforced cementitious materials called Engineered Cementitious Composite (ECC) has been considered for vertical cutoff wall application (Lobbestael, 2014). ECC shows strain-hardening and multiple-cracking behavior, with superior tensile strength and strain capacities (Li, 2019; Wu et al., 2018b, 2019b) compared with normal concrete. More importantly, when loaded beyond the elastic stage, ECC maintains a low hydraulic conductivity due to tight crack width as well as the ability to undergo self-healing (Lepech and Li, 2009; Liu et al., 2016; Yu et al., 2017; Yu et al., 2018; Zhang and Zhang, 2017). In addition, ECC shows excellent durability when exposed to aggressive environment, such as freeze-thaw cycles, hot water immersion, chloride immersion, deicing-salt exposure and highly alkaline environment (Özbay et al., 2013; Van Zijl and Slowik, 2017). Therefore, ECC vertical cutoff walls are expected to be ideal for enhancing seepage control of AMD in tailing dams, especially those that are exposed to seismic load.

Previous works have extensively assessed the tensile ductility, crack width distribution, and mechanical performance of ECC as a potential vertical cutoff wall material for levees (Lobbestael, 2014). Research on the hydraulic conductivity and self-healing performances of ECC is typically conducted in clean water. Hydraulic conductivity of ECC in various environmental exposure conditions (i.e., distilled water, tap water, 60 °C hot water, and Ca(OH)₂ solution) have been reported (Lepech and Li, 2009; Liu et al., 2017; Yu et al., 2017; Zhang and Zhang, 2017). However, no information is available on the contaminant containment performance of ECC. Specifically, data and knowledge on the hydraulic conductivity permeated with AMD and self-healing performance of ECC when exposed to AMD are missing.

To develop sustainable infrastructures with longer service life, several studies have successfully revealed that the self-healing capacity of cement-based materials could be improved by the incorporation of reactive magnesia (MgO) (Qureshi and Al-Tabbaa, 2016; Qureshi et al., 2016, 2018, 2019; Kanellopoulos et al., 2015; Sherir et al., 2016, 2017). The addition of MgO (nearly 4% by weight) results in a binder with rapid setting, good durability and high resistance to chemical attack (Haha et al., 2011; Wu et al., 2018a). An optimum proportion of MgO can enhance the strength of cement-based materials, since the hydration products, brucite (Mg(OH)₂) and hydrotalcite (Mg₆Al₂CO₃(OH)₁₆)-like phases (Ht), in addition to calcium silicate hydrate (C-S-H) and Portlandite (Ca(OH)₂) can effectively densify the matrix (Qureshi and Al-Tabbaa, 2016). The unconsumed MgO in the matrix can act as fillers, which results in a further compaction of matrix and increase in the strength (Chau and Li, 2008). MgO could enrich the content of Ht, as Mg is mainly incorporated in these phases (Wu et al., 2018a; Jin and Al-Tabbaa, 2014a). The effectiveness of hydrotalcite-like phases as adsorbents for metals has been extensively investigated due to their natural anion exchange properties (Jin and Al-Tabbaa, 2014b).

According to ASTM (2016a), the amount of dead burnt MgO should be limited to 6% in cement to avoid material damage caused by delayed expansion, while reactive MgO have minimal impact on the delayed expansion (Sherir et al., 2016, 2017).

The present research aims to investigate the hydraulic conductivity and self-healing performance of ECC and ECC incorporating MgO additive (MgO-ECC) under tap water and AMD conditions. A series of hydraulic conductivity tests, using tap water or field AMD as permeant liquid, were performed on ECC and MgO-ECC specimens preloaded up to 2% uniaxial tensile strain. This mechanical preloading and subsequent exposure to water/AMD environment was intended to simulate a combined mechanical-environmental loading of ECC in mine tailing pond cutoff walls in the field. The self-healing property was assessed by resonant frequency (RF) tests on the pre-cracked specimens subjected to wet-dry cycles. The micro-mechanisms controlling the above macro-properties were interpreted based on analyses of scanning electron microscopy (SEM), Fourier transform infrared spectroscopy (FTIR), X-ray diffraction analysis (XRD) and thermogravimetric analysis (TGA) performed on ECC specimens.

2. Materials and testing methods

2.1. Materials and specimen preparations

The mix proportions of ECC and MgO-ECC are listed in Table 1. Both mixtures consist of Type I Portland cement (PC), ASTM Class F fly ash (FA), tap water, silica sand, polyvinyl-alcohol (PVA) fiber and high range water reducing agents (HRWRA). Type I PC conforming to ASTM (2016a) was obtained from Lafarge (Southfield, MI). Class F FA satisfying ASTM C618 (2012) from Headwaters Resources Inc. (Monroe, MI) was blended into PC with a weight ratio of FA/PC = 1.2. The water/binder (W/B) ratio was fixed as 0.25 as suggested by Li, 2019 in which binder refers to PC plus FA. The fine silica sand with a maximum grain size of 200 μm and an average grain size of 75 μm was chosen to control the mortar matrix fracture toughness (2008). The PVA fiber was manufactured by Kuraray Co., Ltd. The physical properties of PVA fiber are given in Table 2.

The HRWRA produced from W.R. Grace & Co. (Columbia, MD) was used to control the flowability and rheology of the mixtures. The lightly burned MgO (MAGOX® premium grade, 900 °C) with 95.76% purity and 105 s reactivity was used as a supplemental material for ECC. The amount of MgO powder in the mixture was 6% by substitution the weight of PC. The chemical compositions of PC, FA and MgO are listed in Table 3.

The AMD was taken from the borehole as an artesian discharge before entering the Solomon Creek, PA, USA. The AMD was stored in high-density polyethylene bottles supported by Eastern PA Coalition for Abandoned Mine Reclamation (EPCAMR). The AMD chemistry analysis results are summarized in Table 4.

The basic chemistry analysis for AMD was conducted by EPCAMR. The pH (field pH = 5.58), temperature, total dissolved solid, dissolved oxidation and alkalinity were measured by YSI Pro plus multi-parameter water quality probe meter. The electronic conductivity was analyzed by using a Hanna Conductivity probe. Concentrations of Fe, Al and Mn in AMD were measured by a Perkin-Elmer Optima 2000 DV ICP-MS. The sulfate ion concentration was measured by using a Thermo Scientific™ Dionex Ion Chromatography.

Table 1

Mixture proportions of ECC and MgO-ECC (dry weight basis).

Material	Cement	MgO	Sand	Fly ash	Water	HRWRA	Fiber ^a
ECC	1	–	0.8	1.2	0.56	0.007	2
MgO-ECC	0.94	0.06	0.8	1.2	0.56	0.012	2

^a PVA fiber content is by volume (%).

Table 2
Properties of PVA fiber tested in this study.

Length (mm)	Diameter (μm)	Elongation (%)	Density (kg/m ³)	Young's modulus (GPa)	Fiber strength (MPa)
12	39	6	1300	42.8	1600

The preparation of ECC and MgO-ECC mixtures followed a typical ECC mixing procedure as suggested by Huang et al., 2012b. Firstly, all solid ingredients (i.e. Portland cement, fly ash, sand, and/or MgO powder) were mixed without water for 3 min in a 12-L Hobart mixer. Then tap water and HRWRA were added and mixed with solid ingredients for 5 min to achieve a flowable and homogenous slurry. The slurry was casted into dogbone-shaped molds (Fig. 1) and vibrated for 5 min on an electromagnetic vibration table. All specimens were covered with plastic sheet for 24 h before demolding. The demolded ECC and MgO-ECC specimens with void ratios of 11.4% and 10.3% respectively were immersed in tap water tank for 27 days at a room temperature of 20 ± 2 °C to guarantee saturation and eliminate the effects of capillary absorption which may artificially lower the measured hydraulic conductivity (Liu et al., 2016).

2.2. Testing methods

To investigate the hydraulic conductivity of ECC or MgO-ECC under crack-damage conditions, dogbone-shape specimens were preloaded in uniaxial tension to produce multiple crack patterns with various widths for prescribed tensile strains of 0%, 0.5%, 1.0%, 1.5% and 2.0%. The tensile strain refers to the elongation of gage length divided by its initial length (80 mm). The loading procedure followed the Japan Society of Civil Engineers recommended guideline for ECC tensile testing (JSCE, 2008). A controlled displacement rate of 0.5 mm/min was adopted. Two linear variable displacement transducers (LVDTs) were attached on opposite sides of each dogbone specimen to measure the tensile deformation. Crack numbers and widths in all pre-loaded specimens were measured using an infinity X-C21 optical electron microscope with a high resolution of 10 μm (Hirbor CX-50470RZ, Japan), and the collected data were analyzed using the discriminant analysis method to generate crack parameters including width and number as per Li, 2019 and Liu et al. (2016). Triplicate specimens were prepared for each prescribed strain level. The tensile crack patterns of ECC and MgO-ECC specimens were obtained from observed cracks crossing 3 horizontal line (80 mm) drawn in the middle of the specimen along the gage length, as shown in Fig. 2.

Hydraulic conductivity tests were conducted using a falling head setup shown in Fig. 3 (a). To avoid partial closing of cracks of the specimens upon removal from the tensile loading machine, a specially designed displacement-controlled loading device (DCLD) (Fig. 3 (b)) was used to sustain the preloaded tensile strain on the specimen during

Table 3
Chemical compositions of cement, fly ash and MgO used in this study.

Oxide chemistry ^a	PC (%)	FA (%)	MgO (%)
Silicon oxide (SiO ₂)	19.19	38.56	0.31
Aluminum oxide (Al ₂ O ₃)	15.4	17.92	0.2
Sulphate oxide (SO ₃)	2.54	1.86	–
Magnesium oxide (MgO)	3.46	4.35	95.76
Phosphorus oxide (P ₂ O ₅)	–	1.12	–
Potassium oxide (K ₂ O)	0.07	0.97	–
Titanium oxide (TiO ₂)	0.39	1.24	0.01
Ferric oxide (Fe ₂ O ₃)	2.13	9.27	0.13
Calcium oxide (CaO)	54.79	20.92	0.81
Chlorine (Cl)	–	0.01	0.03
Loss on ignition	2.03	3.78	2.75

^a Chemical composition is analyzed by X-ray fluorescence method using ARL9800XP + XRF spectrometry.

Table 4
Chemistry analysis results of AMD sampled from Solomon Creek.

Parameter	Data
pH (field ^a)	5.58
pH (lab ^b)	5.87
Temperature (field) (°C)	15.4
Temperature (lab) (°C)	20.1
Total dissolved solids (mg/L)	2800
Dissolved oxidation (mg/L)	2.0
Total alkalinity (mg/L)	106
Electronic conductivity, μS/cm	1390
Sulfate ion (mg/L)	640
Ferric iron (mg/L)	1900
Ferrous iron (mg/L)	190
Aluminum (mg/L)	1.2
Manganese (mg/L)	17

^a pH is measured in the borehole by YSI Pro plus multi-parameter water quality probe meter.

^b pH is measured in the laboratory by Hanna Instruments HI 9313-6 portable pH/E/C meter;

the entire hydraulic conductivity measurements. It is noted that the DCLD could yield a constant preloaded tensile strain on cracked specimens during the hydraulic conductivity tests. Each specimen was then configured within the DCLD, and then it was horizontally sandwiched between two Plexiglas water tanks (Fig. 3 (a)). The two Plexiglas water tanks were cuboid with inner-size of the cross-section (2400 mm²). Rubber seals were inserted between the Plexiglas water tank and the tension specimens to ensure water-tightness.

The setup procedures for retaining the specimens in loaded condition and details of hydraulic conductivity testing setup were described in Liu et al. (2016). The hydraulic conductivity test was conducted at a standard room temperature of 20 ± 2 °C. The porosity of tested specimens was calculated based on the dry density and specific gravity of the tested specimens. The specific gravity of ECC and MgO-ECC was 1.94 and 1.95, respectively. The hydraulic head was continuously monitored and recorded for 2 h immediately after the upper water tank was filled by tap water or AMD, and then it was daily measured up to a steady-state (Liu et al., 2016; Yu et al., 2017). The hydraulic conductivity (k) was calculated following ASTM (2016b) using the recorded water falling head data as shown in Eq. (1):

$$k = \frac{a \times L}{A \times t_f} \ln \left(\frac{h_0}{h_f} \right) \quad (1)$$

where k is the hydraulic conductivity (m/s); a is the cross-section of the standpipe (69.4 mm²); L is the thickness of the specimens (12.7 mm); h_0 and h_f are initial and final water heads in standpipe (mm), respectively; A is the cross-section area of the specimens subjected to water flow (2400 mm²); and t_f is the test duration in second (s).

The hydraulic termination criteria of hydraulic conductivity were in accordance with ASTM (2016b) when the specimens were permeated with tap water, that was (1) the ratio of outflow to inflow was within 0.75 to 1.25, and (2) four or more consecutive hydraulic conductivity values fell within $\pm 25\%$ or better of the mean value and the plot of

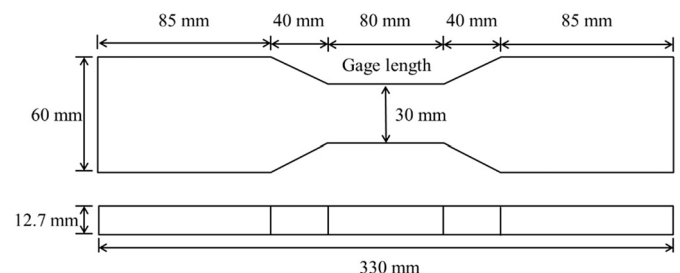


Fig. 1. Dimensions of the dogbone specimen for uniaxial tension test.

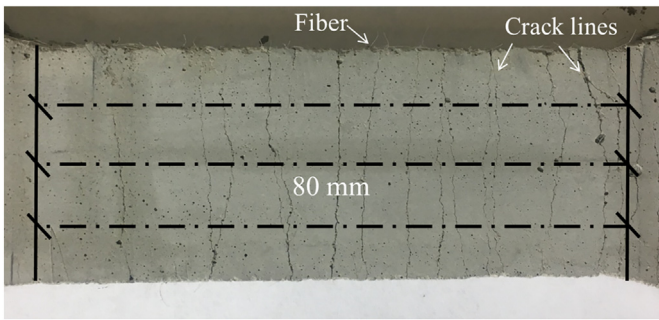


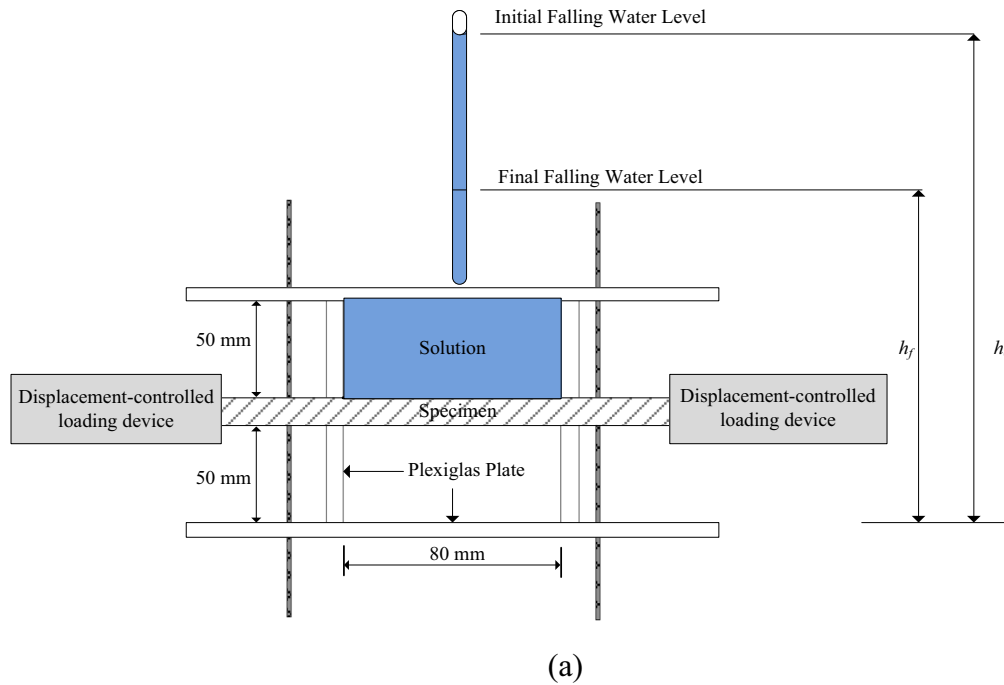
Fig. 2. Cracked pattern of MgO-ECC specimen at 2% tensile strain.

the hydraulic conductivity versus time showed insignificant upward or downward trend. For the specimens permeated with AMD, the outflow effluents were collected from the lower water tank for volume, pH and electrical conductivity (EC) analyses. Measurement of each pH and EC was conducted twice using a portable pH/EC meter (Hanna Instruments HI 9313-6). The chemical equilibrium was assessed by comparing the

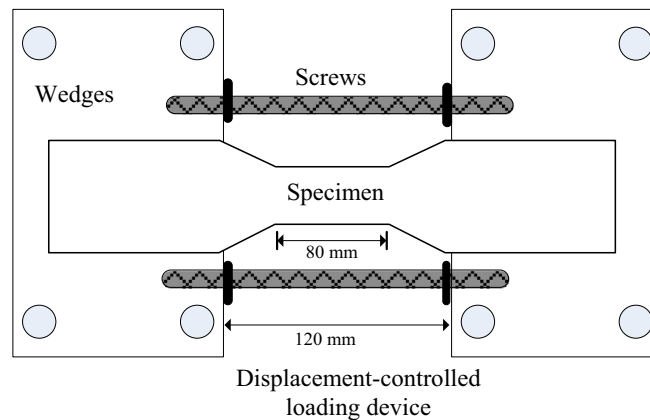
pH and EC in the effluent with those in the influent as per ASTM D 7100 (2011).

The wet-dry cycles were used as an accelerated testing method to simulate field scenarios in which ECC cutoff walls are subjected to frequent fluctuation of the groundwater level due to seasonal variations (Shen et al., 2017; Wu et al., 2019c). The specimens with preloaded tensile strains of up to $\sim 2.0\%$ were subjected to wet-dry cycles consisting of immersing the specimens in an acid-resistant plastic storage tank with AMD (pH = 5.87) or tap water (pH = 8.13) for 24 h, and then followed by drying the specimens in a room condition ($20 \pm 2^\circ\text{C}$, $50 \pm 5\%$ relative humidity) for 24 h. The solution in the tank was periodically renewed after each cycle and the ratio of solid-liquid volume is kept constant at 1:500. After each wet process prior to the next consecutive dry process, the specimens were moved from the AMD or tap water, and the remaining liquid on the surface of the specimens was carefully wiped off using filter papers.

As a rapid and nondestructive testing technique, the resonant frequency (RF) measurement is used to quantify the damage and self-healing in ECC materials (Yang et al., 2009, 2011). The RF measurements were conducted using a Resonance Tester (RT-1) system in accordance



(a)



(b)

Fig. 3. Falling head hydraulic conductivity testing setup: (a) sketch of falling head hydraulic conductivity testing setup and (b) displacement-controlled loading device.

with ASTM C215 (2008) for evaluating damage of the specimens. The RF measurements were taken before and after the specimen preloading (strain = 0.5–2.0%) to record the decrease in RF values. The preloaded specimens after each wet-dry cycle were also subjected to RF test to evaluate the rate of self-healing reflected by increase in RF values. After each wet-dry cycle, the crack width of the specimens was observed using the Infinity X-C21 electron microscope equipped with high-performance zoom lens (Hirbor CX-50470RZ, Japan).

After RF measurement, the self-healed specimens for micro-analysis were carefully scratched on the crack lines with a stainless-steel razor after the completion of wet-dry cycle. Approximate 2 g of each specimen was extracted and air-dried powder specimen was subjected to the FTIR, XRD and TGA tests. The FTIR tests were conducted with a mid-infrared thermo scientific spectrometer (Nicolet 6700) at 4 cm^{-1} scanning resolution. The XRD tests were conducted on RigakuD/Max-2500 using a Cu-K α source with a wavelength of 1.5405 Å. The instrument was operated at 40 kV and 20 mA. A step size of $2\theta = 0.02^\circ$ and a scanning speed of 5 s/step are used. Specimens were analyzed over a range of 2θ from 5° to 60° . The TGA tests were analyzed with a thermogravimetric analysis (Model Q500 with helium, TA instruments, New Castle Delaware). The TGA test was started from 30 to 1000 °C with an increasing rate of 5 °C/min. Approximate 1 cm³ sample on the interior of cracks of ECC or MgO-ECC specimen subjected to RF measurement was carefully cut, frozen using liquid nitrogen (−195 °C) and followed by sublimating the frozen water at a −80°C environment. The sample was then subjected to SEM analyses by using a 5 kV accelerating voltage high resolution device (HITACHI S4800). The conductive coating for the sample was not used in this study for eliminating noise signal.

3. Experimental results

3.1. Tensile crack patterns

Table 5 shows the crack patterns of ECC and MgO-ECC at various tensile strains. As expected, for ECC and MgO-ECC, both crack width and crack number increase with an increase in tensile strain. The crack width increases initially but appears to stabilize beyond about 1% strain. Overall, the multiple cracking behaviors of ECC materials with self-controlled crack width are different from normal concrete in which only one localized crack is generated under tension and the crack width increases indefinitely with increasing tensile strain (Li et al., 2008). The formation of multiple cracks instead of a localized large crack is beneficial for maintaining low hydraulic conductivity of ECC even in the cracked stage (Liu et al., 2016).

It is also observed that the average crack width of MgO-ECC is 8.7% to 30.3% less than that of ECC in the tensile strain range of 0.5% to 2.0%. The crack numbers of MgO-ECC is 7.7% to 28.6% more than that of ECC for the same tensile strain range. In principle, the total crack width should equal the product of the gage length and

the tensile strain. However, the data shows that the total crack width is below this expected value. This may be attributed to the recovery of localized opening displacement after unloading of cracks and the limited resolution of optical electron microscope. The tighter cracks result in lower hydraulic conductivity, which is further discussed in the “Discussion” section.

3.2. Recovery of resonant frequency

The change of RF value for preloaded specimens after each cycle under tap water and AMD is shown in Fig. 4. The solid points in these plots indicate the RF value of control group of un-cracked specimens that have undergone the same conditioning regime. The observed slight increase in RF value of control group specimens is due to continued hydration of matrix materials (Yang et al., 2009). For the specimens preloaded with higher initial tensile strain, a lower initial RF value is observed which is attributed to the larger crack widths and higher crack numbers. As the tensile strain increase from 0% to 2%, the RF value drop 64.07% and 52.11% for the ECC and MgO-ECC, respectively. It indicates that the MgO-ECC exhibit higher integrity than ECC under the same tensile strain. The RF value of the MgO-ECC is 2.97% and 6.86% higher than ECC before and after wet-dry cycles, respectively. Moreover, the AMD exhibits almost no effect on the RF values for the specimens of ECC and MgO-ECC as compared to tap water for the same number of wet-dry cycles.

There is a clear tendency that the RF values initially increase rapidly with the number of wet-dry cycles, but eventually level off. It indicates that the recovery of specimens occurs with increasing wet-dry cycles. For the ECC specimens, the threshold cycle numbers before the RF reached a steady state value are estimated as 5 for tap water exposure condition and 6 for AMD exposure condition; whereas the corresponding threshold cycle numbers are found to be 3 (tap water exposure) and 6 (AMD exposure) for the MgO-ECC specimens. This phenomenon indicates that the MgO-ECC pose a higher recovery rate than ECC under the tap water exposure condition.

To quantitatively assess the recovery RF, the recovery ratio (R_{RF}) is calculated according to the following equation:

$$R_{RF} = \frac{RF_\varepsilon}{RF_0} \quad (2)$$

where RF_ε is the RF value of preloaded specimens under tensile strain ε ($\varepsilon = 0.5\%–2.0\%$) exposed to tap water or AMD. The RF_0 is the RF value of un-cracked specimens when exposed to tap water or AMD. A higher R_{RF} value reflects higher recovery ability.

Table 6 summarizes the R_{RF} of ECC and MgO-ECC before and after the 12th wet-dry cycle. As show in Table 6, the R_{RF} of preloaded ECC and MgO-ECC falls from 72.73% to 35.93% and from 79.32% to 47.89%, respectively, as tensile strain increases from 0.5% to 2.0%. After the 12th wet-dry cycle, the R_{RF} values under tap water and AMD conditions at the tensile strain of 0.5 to 1.5% are approximately the same for both ECC and MgO-ECC specimens. In contrast, at the tensile strain of 2.0%, both ECC and MgO-ECC specimens possess lower R_{RF} values under the AMD exposure condition as compared to tap water exposure condition. The above phenomenon indicates that both ECC and MgO-ECC specimens possess approximately the same recovery ability at the tensile strain of 0.5 to 1.5% regardless of the type of exposure liquid (tap water versus AMD); whereas they display lower recovery magnitude of R_{RF} under AMD exposure condition relative to that under tap water exposure condition. It is interesting to see the MgO-ECC specimen display higher R_{RF} values than ECC specimens irrespective of type of testing liquid which is more notable at 2% tensile strain, indicating higher self-healing ability of MgO-ECC specimens.

Table 5
Crack widths and numbers of preloaded ECC.

ECC mixture	Tensile strain (%)	Avg. crack width (μm) (coefficient of variation)	Max. crack width (μm)	Avg. no. of cracks	Total crack width (μm)
ECC	0	0	0	0	0
	0.5	24.33 (1.3%)	32	6	145.96
	1.0	34.91 (1.1%)	44	14	488.74
	1.5	36.96 (2.1%)	56	18	665.28
	2.0	38.46 (2.5%)	62	26	999.96
MgO-ECC	0	0	0	0	0
	0.5	20.52 (2.1%)	31	7	143.64
	1.0	24.33 (3.5%)	45	18	437.94
	1.5	29.14 (3.3%)	53	22	641.08
	2.0	35.12 (2.8%)	59	28	983.36

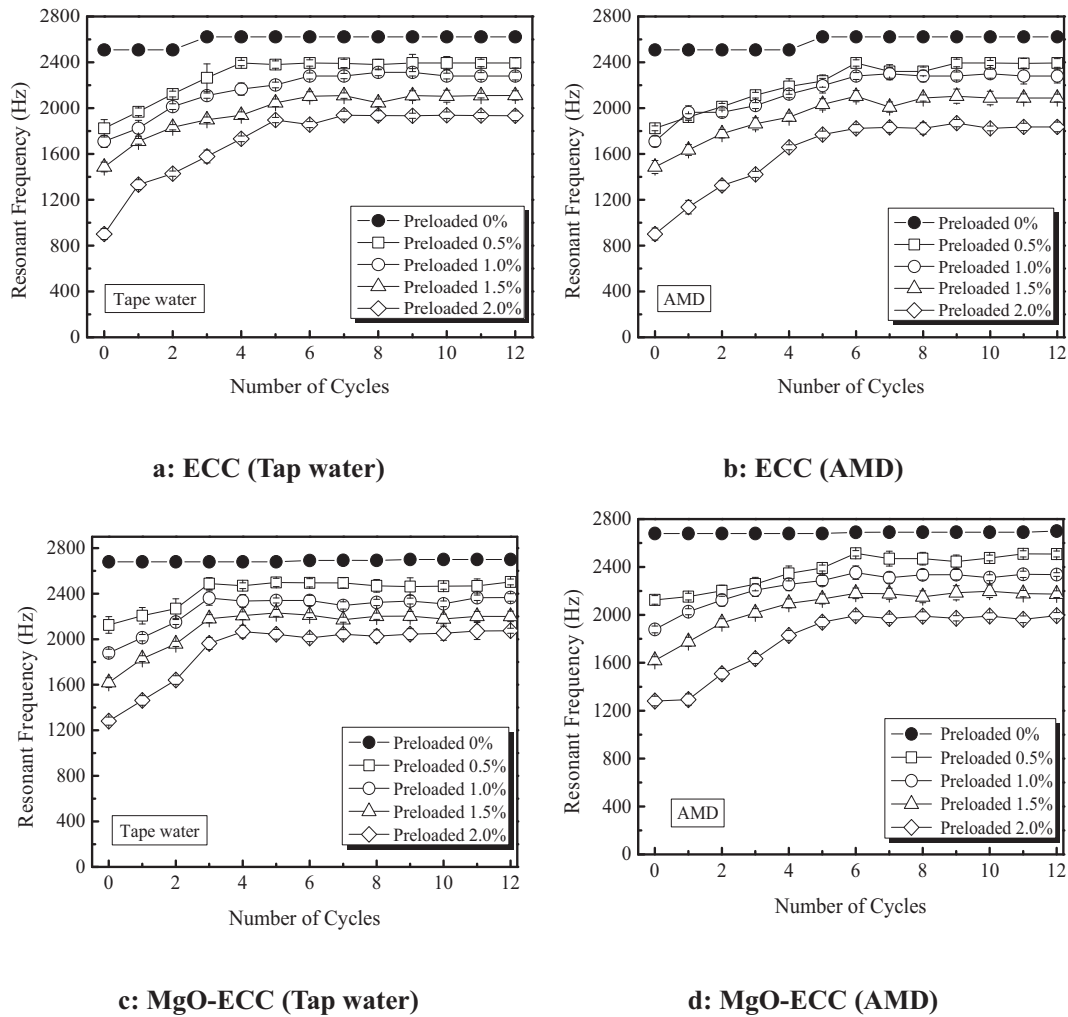


Fig. 4. Resonant frequency of ECC and MgO-ECC changed with wet-dry cycles.

3.3. Crack healing phenomenon

Typical visual crack sealing patterns of ECC and MgO-ECC over wet-dry cycles times are presented in Fig. 5. In each mix combination and solution, crystalline crack sealing is observed after 12 wet-dry cycles. Most of the fine cracks in ECC specimens are sealed after 4 cycles under the tap water exposure condition, whereas it takes about 6 cycles under AMD exposure condition. It is seen that the cracks in MgO-ECC specimens are almost sealed after 2 and 6 wet-dry cycles under tap water and AMD exposure conditions, respectively. Clearly the addition of MgO to ECC has yielded a positive effect on the crack sealing over the wet-dry cycles, especially under exposure to AMD.

Table 6 Recovery ratio (in percentage) of ECC and MgO-ECC specimens before and after exposed to the 12th wet-dry cycle.

Preloaded tensile strain		0.5%	1.0%	1.5%	2.0%	
Before wet-dry cycles	ECC	72.73	68.18	59.25	35.93	
	MgO-ECC	79.32	70.24	60.40	47.89	
After 12th wet-dry cycle	Tap water	ECC	91.30	86.96	80.47	73.72
		MgO-ECC	93.41	88.33	82.17	77.49
	AMD	ECC	91.29	86.98	79.63	70.02
		MgO-ECC	93.61	87.28	81.11	74.47

3.4. pH and EC properties for un-cracked specimens

Fig. 6 (a and b) shows the pH and EC equilibrium status of the out-flow and inflow for the un-cracked ECC and MgO-ECC (tensile strain = 0%) permeated with AMD. The porosity of ECC is larger than MgO-ECC (Fig. 6a). For the AMD permeation liquid, the pH in effluent slightly and gradually increases while the EC decreases with increasing pore volume of flow (PVF). The PVF refers to the volume of effluent divided by the volume of voids in the ECC or MgO-ECC specimen. The observations are attributed to: (1) neutralization of free H⁺ in AMD by the OH⁻ released from the hydration products (i.e., Ca(OH)₂, C-S-H and Mg(OH)₂) in the ECC and MgO-ECC, which leads to a slight increase in the effluent pH with increasing PVF, and (2) precipitation reaction between certain amount of cations (i.e., Fe²⁺/Fe³⁺) in AMD and OH⁻ released from the hydration products formed in the matrix of ECC and MgO-ECC specimens, which leads to the decrease in EC with increasing PVF. The pH_{out}/pH_{in} of the ECC and MgO-ECC varies from 1.72 to 1.85 and 1.73 to 1.86 as PVF increases from 0.17 to 0.80, respectively. The values of pH_{out}/pH_{in} are not consistent with the target range of 0.9 to 1.1 (Fig. 6b), and therefore pH equilibrium has not been reached at the end of test. The EC_{out}/EC_{in} of the ECC and MgO-ECC decrease from 1.12 to 0.92 and 1.09 to 0.91 as the PVF increases from 0.38 to 0.8, respectively. The values of EC_{out}/EC_{in} fall in the target range of 0.9 to 1.1 (Fig. 6b), indicating that EC equilibrium is deemed to have reached at day 39.

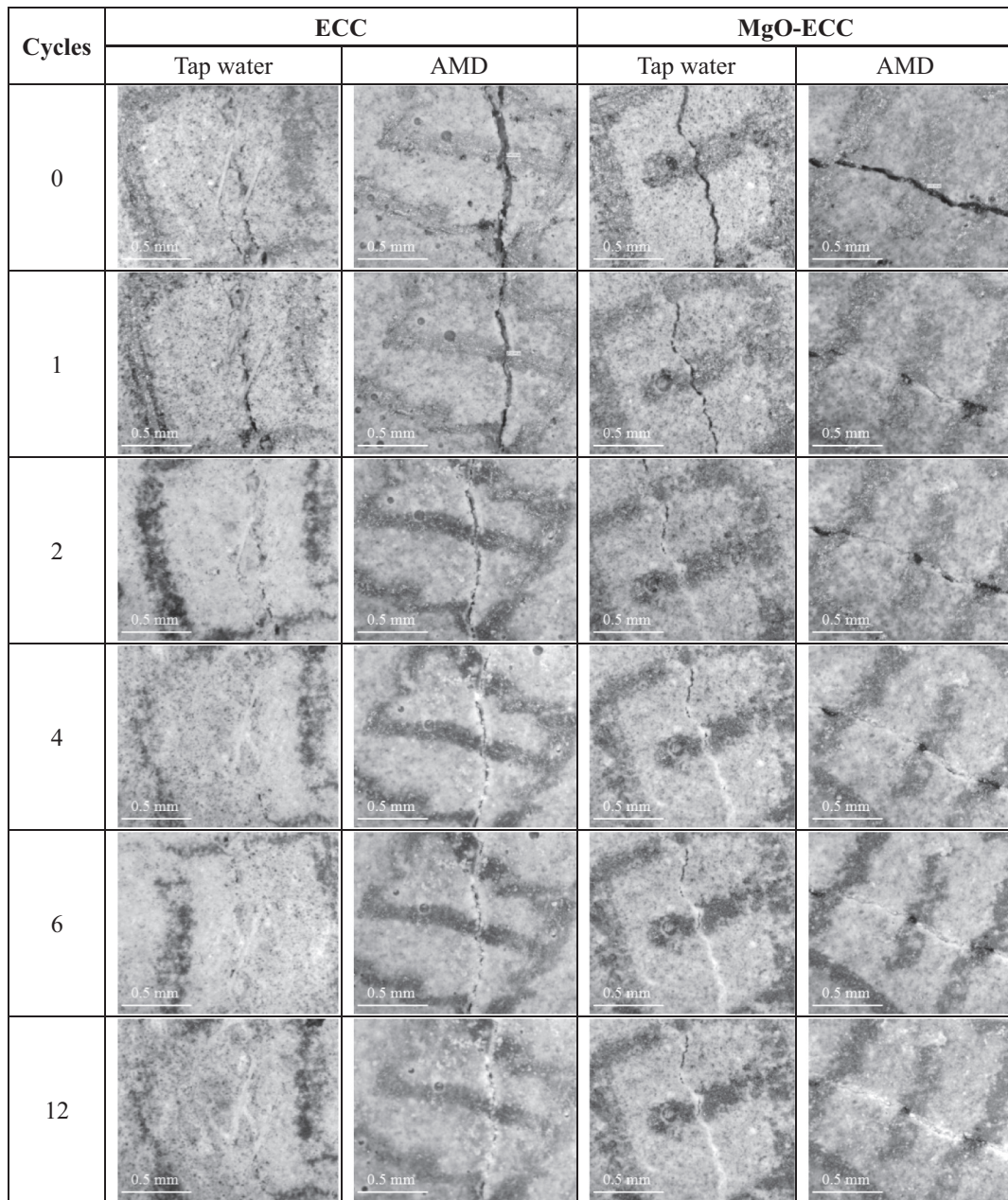


Fig. 5. Typical crack sealing pattern of ECC and MgO-ECC from 0 to 12 wet-dry cycles (tensile strain = 2.0% and initial crack width = 35.2–40.8 μm).

3.5. Short-term hydraulic conductivity

The hydraulic conductivity value exhibits insignificant upward or downward trend after 39 days (Fig. 7 (a and b)). The hydraulic conductivity (k_w) of un-cracked ECC and MgO-ECC specimens (strain = 0%) decrease sharply and then stabilize at the 2.85×10^{-12} m/s and 2.42×10^{-12} m/s, respectively. The un-cracked ECC and MgO-ECC specimens (strain = 0%) possess hydraulic conductivity (k_c) of 4.51×10^{-12} m/s and 3.12×10^{-12} m/s, respectively, when permeated with AMD at a PVF of 0.80 and 0.76 respectively. It is seen in Fig. 7 that both k_w and k_c drop sharply at the beginning stage (PVF = 0 to 0.3) and then eventually levels off. The phenomenon is attributed to the continued hydration and filling of matrix pore space by the formed hydration products during the permeating.

The hydraulic conductivity of cracked specimen is much higher than that of un-cracked specimen. This is because of the fact that

the hydraulic conductivity of concrete scaled with the 3rd power of crack width (Wang et al., 1997). Thus, the cracked specimens could reach the hydraulic equilibrium (i.e., hydraulic termination criteria prescribed by ASTM (2016b)) much faster than the un-cracked specimens. While hydraulic equilibrium is assured when the test was terminated at 39 days, it is not clear that self-healing is complete in the cracked ECC and MgO-ECC specimens. Fig. 8 ((a) and (b)) shows the hydraulic conductivities of ECC and MgO-ECC specimens permeated with tap water (k_w) and AMD (k_c) for 39 days under the preloaded strain condition (strain = 0–2.0%). It is noted that the measured k_w and k_c values of cracked specimens reflect a combined effect of crack and self-healing, although the magnitude of self-healing at the termination and full self-healing were not explored in this study. For comparing with the results of previous research, the hydraulic conductivity for ECC is normalized by the crack number as also shown in Fig. 8 (a and b).

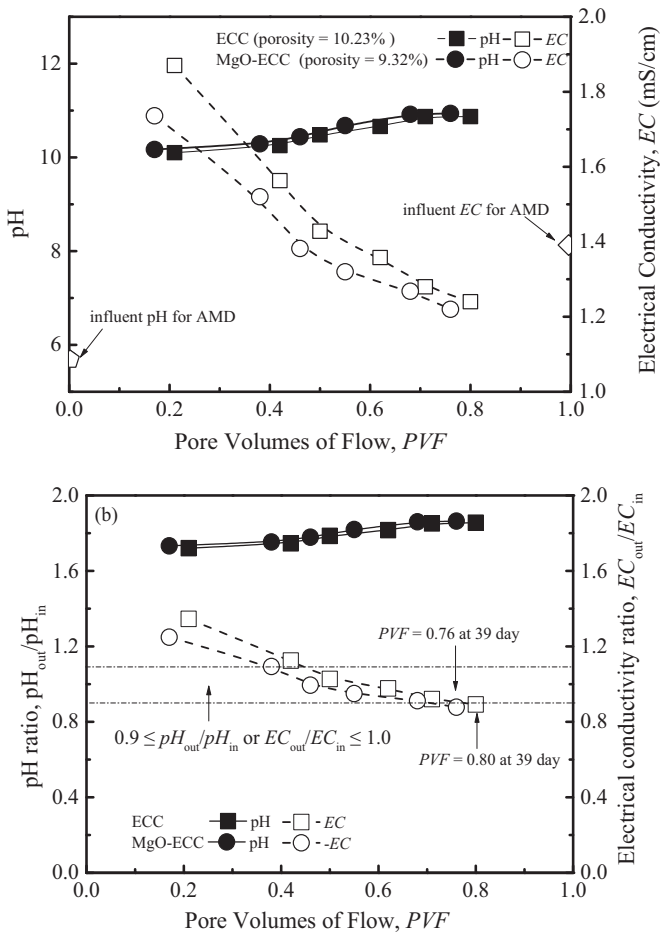


Fig. 6. pH and EC versus pore volumes of flow (PVF) during hydraulic conductivity tests permeated with AMD: (a) pH and EC value and (b) pH and EC equilibrium status.

There is a clear trend that hydraulic conductivity (k_w and k_c) increases with increasing tensile strain for both mixtures. The results of hydraulic conductivity of ECC are insignificantly different between tap water and AMD permeation. The MgO-ECC shows practically the same hydraulic conductivity with ECC at all strain levels (strain = 0–2.0%). The hydraulic conductivities of all cracked specimens at the strain level of 0.5% to 2.0% are higher than commonly accepted limits (1.0×10^{-8} m/s) for most vertical cutoff walls, while the magnitude of hydraulic conductivity of un-cracked specimens (10^{-12} m/s) is much lower than the commonly accepted limits. It is also observed that the hydraulic conductivity of specimens with preloaded tensile strains in the range 0.5%–1.0% maintains a constant value of 10^{-8} m/s. As the tensile strain increases to 2.0%, the hydraulic conductivity of ECC and MgO-ECC specimens permeated with AMD measures as 6.71×10^{-7} m/s and 3.93×10^{-7} m/s, respectively. Moreover, the hydraulic conductivity of MgO-ECC is 57.84% and 49.8% lower than ECC as the specimens exposed to tap water and AMD, respectively. After normalized by the number of cracks, the hydraulic conductivity of ECCs and MgO-ECCs specimens drop one to two magnitudes. It is also observed that the normalized k_w and k_c values of both ECC and MgO-ECC at tensile strain of 0.5% are slightly higher than their corresponding values at tensile strain of 1.0%. This is attributed to the crack numbers of ECC and MgO-ECC at tensile strain of 1.0% are 133% and 157% higher than those at tensile strain of 0.5%, respectively.

For comparison with data in the literature, the normalized hydraulic conductivities of un-cracked and cracked ECC permeated with tap water and 3% NaCl solution at different pre-load tensile strain levels are summarized in Fig. 9 and Table 7. The hydraulic conductivity in Lepech and Li (2009) are much lower than those in others, which may be due to that

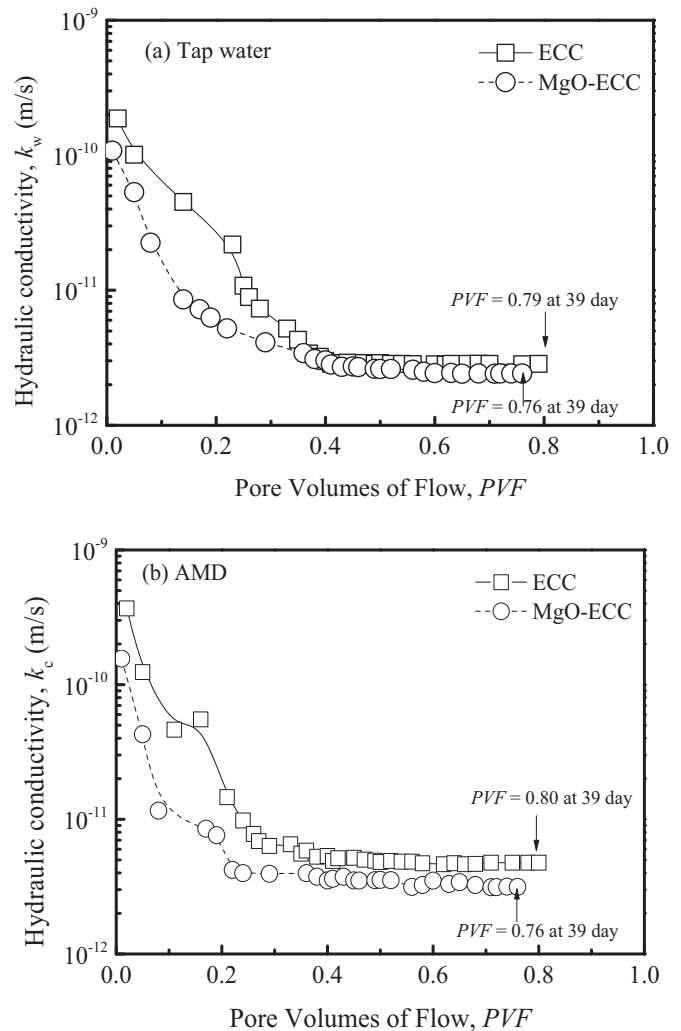


Fig. 7. Hydraulic conductivity versus pore volumes of flow (PVF) during hydraulic conductivity tests permeated with (a) tap water and (b) AMD.

their hydraulic conductivity was obtained when full self-healing was achieved. A regression analysis is conducted for identifying the correlation between hydraulic conductivity and preloaded tensile strain. The derived equations are also presented with regression line as shown in Fig. 9. The equation can be used to predict the hydraulic conductivity of ECC within the range of tensile strain presented in this study. Most of the data presented in the figure are covered within the upper and lower boundary lines, which represent a changing tendency of hydraulic conductivity with respect to the tensile strain. It is seen that the hydraulic conductivity of ECC tends to increase rapidly as the tensile strain increases from 0% to 0.5%, while the change is small when the tensile strain ranges from 0.5% to 2.0%. It is seen from Fig. 9 that the normalized hydraulic conductivities of ECC and MgO-ECC are lower than the commonly accepted limits (1.0×10^{-8} m/s) at a tensile strain level lower than 1.32%, which is derived from the regression equation for this study (y_0). It should be noted that the regression line is only valid under the current experimental conditions.

3.6. X-ray diffraction analysis

XRD tests are shown in Fig. 10. The presence of C-S-H, C_2S , C_3S , calcite ($CaCO_3$), ettringite (Aft) and hydroxalite-like phase (Ht) was confirmed with the characteristic XRD peak irrespective of type of testing liquid. For both ECC and MgO-ECC specimens, formation of poorly crystalline C-S-H is detected at $2\theta \approx 26.8^\circ$, 29.5° and 49.0° , identified as the

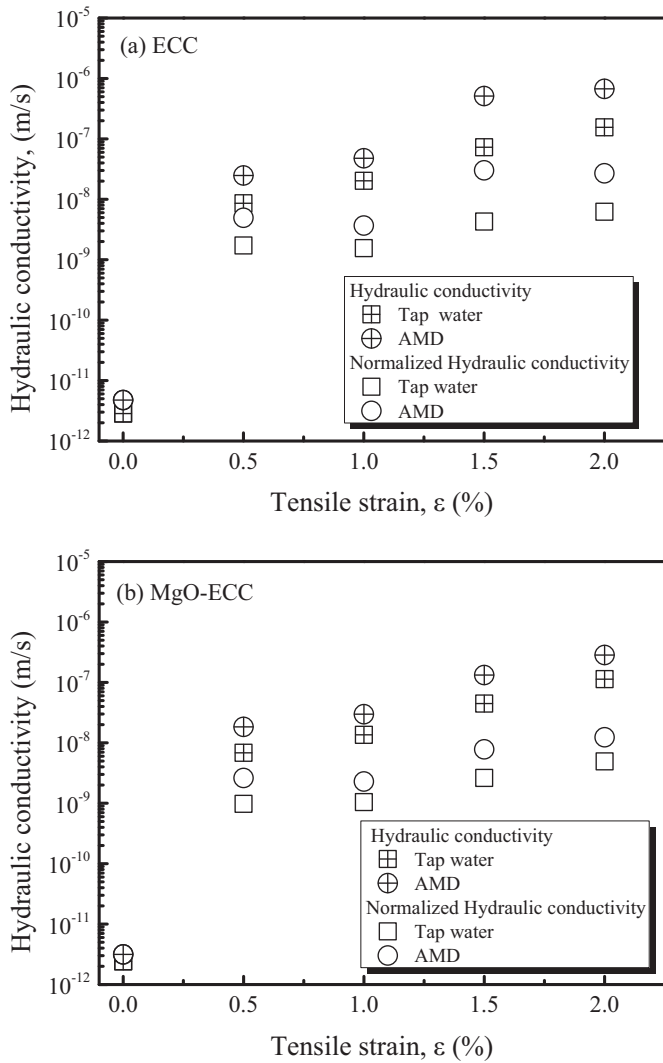


Fig. 8. Hydraulic conductivity and normalized hydraulic conductivity of specimens permeated with tap water and AMD versus preloaded tensile strain: (a) ECC and (b) MgO-ECC.

self-healing products at the early curing age (Wu et al., 2012; Du et al., 2014). The $\text{Ca}(\text{OH})_2$ is identified at 36.0° , 45.8° and 47.5° , which is consistent with the observations reported by Qureshi and Al-Tabbaa

(2016). The influence of MgO additive on the formation of self-healing products is confirmed with the major brucite ($\text{Mg}(\text{OH})_2$) peaks at 18.5° and 37.5° , and the characteristic peaks of hydromagnesite at 32.2° and 42.8° , which is consistent with previous studies (Qureshi and Al-Tabbaa, 2016; Jin and Al-Tabbaa, 2014a; Wu et al., 2012). Furthermore, the formation of Ht is confirmed with the characteristic peaks at 22.8° and 39.6° , which agrees well with previous studies dealing with MgO mixtures (Qureshi and Al-Tabbaa, 2016; Jin and Al-Tabbaa, 2014b; Wang and Scrivener, 1995; Song and Jennings, 1999). The characteristic peaks of hematite (Fe_2O_3) are reflected at 53° (Shettima et al., 2016) in specimens subjected to the AMD, indicating that free ferrous iron and ferric iron in the AMD (Table 4) precipitate on the crack surface. The AFt may exist in the matrix as its peak is detected at 42.5° , which is consistent with the observations reported by Huang et al. (2012a, 2012b). Regarding to the AMD condition, the peaks at 45.8° and 50.5° are disappeared due to that free H^+ from the AMD might have dissolved $\text{Ca}(\text{OH})_2$ and calcite originated from the self-healing hydration products. The C-S-H peak at 26.8° in ECC and MgO-ECC are found to have lower intensity in AMD than in tap water, indicating that AMD exposure has yielded lower hydration reactions.

3.7. Fourier-transform infrared spectroscopy analysis

Fig. 11 presents the FTIR graph of self-healing products from the ECC and MgO-ECC specimens after wet-dry cycles under tap water and AMD exposure conditions. Similar infrared bands can be observed from the four specimen types. The characteristic H-O-H bond stretching is noticed around 1650 , 3460 and 3620 cm^{-1} followed by shallow wide transmittances, which indicates the presence of $\text{Ca}(\text{OH})_2$ and $\text{Mg}(\text{OH})_2$ (Qureshi and Al-Tabbaa, 2016). The presence of ettringite is confirmed by the sulfate ($-\text{SO}_4^{2-}$) stretching vibration around 1116 cm^{-1} (Qureshi and Al-Tabbaa, 2016). The Si-O bond stretching is noticed around 980 cm^{-1} , which indicating the presence of silica gel (C-S-H) (Fernández-Jiménez and Palomo, 2005). The -Si-O-Mg bond and -Al-O/OH bond stretching is around 530 and 690 cm^{-1} , respectively, indicating that the presence of Ht (Huang et al., 2012a, 2012b).

3.8. Scanning electron microscopy

Fig. 12 (a)–(d) shows the SEM image of the self-healing products in ECC and MgO-ECC specimens subjected to 12th wet-dry cycles under tap water and AMD conditions. For the ECC specimens, the self-healing products are blocky-like calcite as shown in Fig. 12 (a), (b), which has been identified as one of the self-healing products in cracked ECC (Zhao, 2012). As shown in Fig. 12 (c), (d),

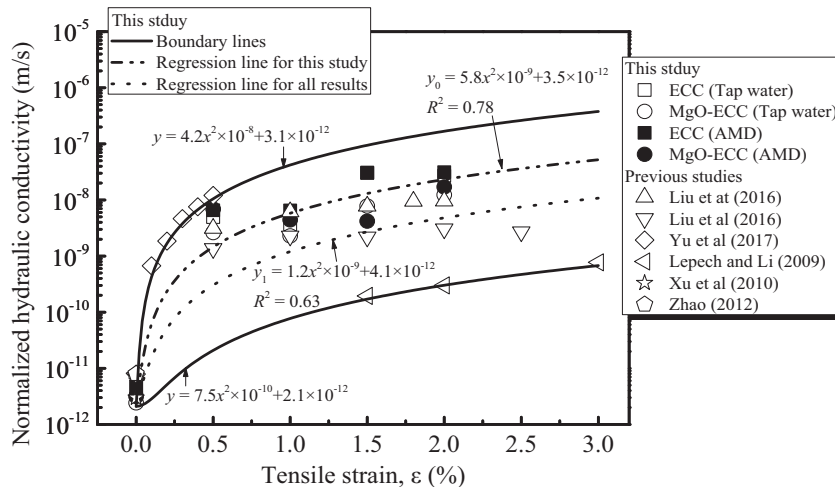


Fig. 9. Fitting equations of normalized hydraulic conductivity for ECCs obtained from this study and previously published studies.

Table 7
Summary of basic information of hydraulic conductivity studies for various ECC reported in previous studies.

Material	Water/binder	Curing time (days)	Prescribed strain level (%)	Crack number	Permeated liquid	Reference
Normal ECC ^a	0.25	28	0–2.0	8–24	Tap water	(Liu et al., 2016)
Crumb rubber ECC	0.25	28	0–2.5	11–48	Tap water	(Liu et al., 2016)
Normal ECC	0.4	28	0–3.0	47–87	Tap water	(Lepech and Li, 2009)
Normal ECC	0.22	28 and 56	0	0	3% NaCl solution	(Xu and Cai, 2010)
Normal ECC	0.3	28	0–0.5	0–5	Tap water	(Yu et al., 2017)
Normal ECC	0.22	28	0	0	3% NaCl solution	(Zhao, 2012)

^a The material composition of normal ECC is consistent with that of the ECC used in this study. All specimens have the same cross-section area of 24 mm²

CaCO₃, hydromagnesite and flaked-like brucite appear in the MgO-ECC specimens, which is similar with findings reported by other researchers (Qureshi and Al-Tabbaa, 2016). Regarding the AMD condition, ettringite can be seen in the MgO-ECC specimen. Based on Fig. 12(d), the diameter of needlelike ettringite is estimated to be approximately 0.6–1.1 μm, which is consistent with the pre-view study (Scrivener et al., 2016).

3.9. Thermogravimetric analysis

Fig. 13 shows the TGA and differential thermogravimetric (DTG) curves for the self-healing products in ECC and MgO-ECC specimens subjected to the 12th wet-dry cycle using tap water and AMD as immersing liquids. The loss of hygroscopic water corresponding to the temperature of 50 to 200 °C is arbitrarily used to represent the C-S-H (Haha et al., 2011). The temperature range of 300 to 500 °C includes mainly the decomposition of Ht (Scrivener et al., 2016). Based on the DTG curves, the mass loss around ~425 °C is attributed to the non-evaporable water detached from Mg(OH)₂ and/or Ca(OH)₂, and the mass loss of CO₂ from 550 to 850 °C is confirmed to the decomposed carbonate-containing phases including hydromagnesite and calcite (Scrivener et al., 2016). The weight loss between 400 and 450 °C and 550–850 °C is denoted as Δm₁ and Δm₂ respectively and their values are shown in Table 8. It can be seen that the MgO-ECC specimen has higher Δm₁ (1.69%) than the ECC one (0.51%) as exposed to tap water, which is attributed to the formation of Mg(OH)₂ as one of the MgO-ECC self-healing products in addition to Ca(OH)₂. When exposed to AMD, the Δm₁ values of MgO-ECC and ECC drop to 0.91% and 0.38%, respectively. Similar changing patterns are found on Δm₂. Free H⁺ from the AMD might have dissolved the Ca(OH)₂, Mg(OH)₂ and carbonate-containing phases originated from the self-healing hydration products, which is consistent with the XRD results.

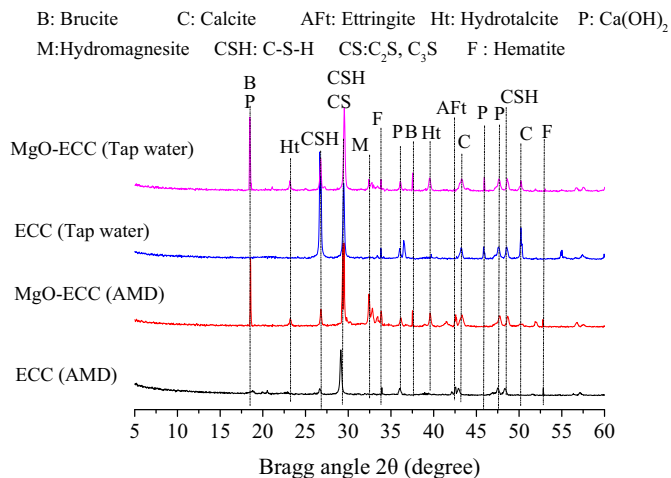


Fig. 10. X-ray diffractograms of conducted on crack lines of ECC and MgO-ECC subjected to the 12th wet-dry cycle using tap water and AMD as immersing liquids.

4. Discussion

ECC exhibits multiple cracking behaviors with slow increase in the crack width accompanied by rapid increases in the crack number after 1.0% tensile strain (Li, 2019). As shown in Fig. 8, ECC is expected to maintain low hydraulic conductivity due to: (1) the width of the multiple cracks of ECC under tension can be controlled to a low value, which is typically lower than 60 μm (Lepech and Li, 2009), and even below 40 μm in the present study (Table 5). Previous study has shown that the hydraulic conductivity of cracked materials increases cubically with increasing crack width and linearly with increasing crack number (Wang et al., 1997), and (2) the self-healing properties of cracks within the ECC also contributes to reducing the hydraulic conductivity of cracked ECC (Lepech and Li, 2009; Edvardsen, 1999). Compared to tap water condition, AMD produces an acidic environment and dissolves part of calcite, brucite and Portlandite originated from the self-healing hydration products (Figs. 10 and 13), which results in slightly higher observed hydraulic conductivity (Fig. 8). Incorporation of MgO in ECC leads to tighter average crack width that is more notable at a tensile strain of 2.0% (Table 5), resulting in a lower hydraulic conductivity although the micromechanics are not fully explored.

Regarding the self-healing of ECC and MgO-ECC in the tap water condition, it can be found that: (a) further hydration of the unreacted cement or fly ash produces new C-S-H (Figs. 10–13) on the interior of the crack of ECC and MgO-ECC; (b) the free calcium ions dissolved from ECC and MgO-ECC cementitious matrix react with dissolved carbon dioxide during the wet-dry cycles to yield formation of calcium carbonate or hydroxide (Figs. 10–13). The chemical reactions are expressed by Eqs. (3) and (4) (Wu et al., 2012); and (c) the presence of MgO results in considerable formation of Mg-rich products such as brucite, hydromagnesite, Mg-rich calcite and hydrotalcite-like phases in the crack of MgO-ECC (Figs. 10–13). These reactions can be expressed

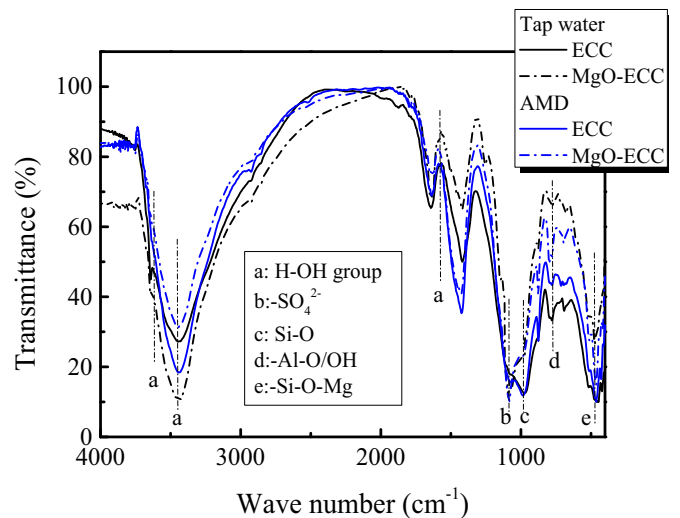


Fig. 11. FTIR images conducted on crack lines of ECC and MgO-ECC after subjected to the 12th wet-dry cycle using tap water and AMD as immersing liquids.

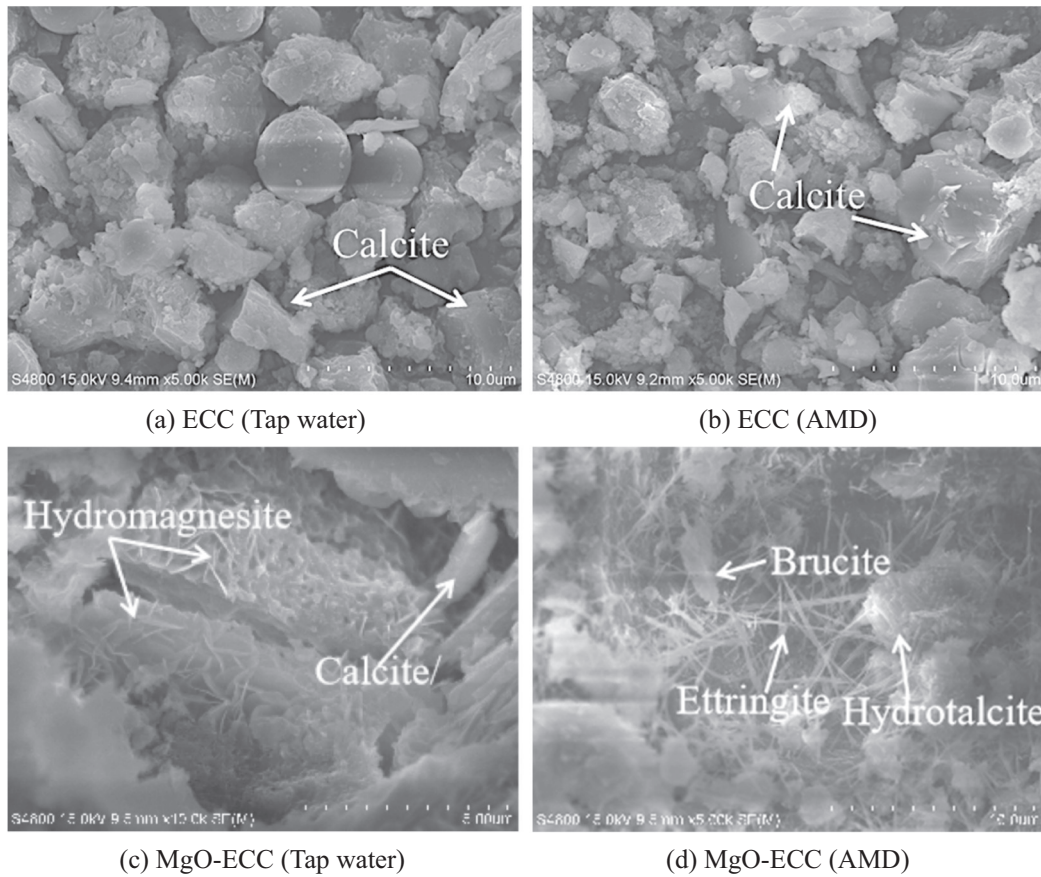
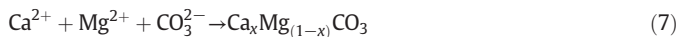
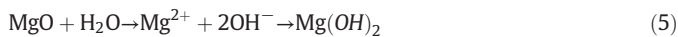
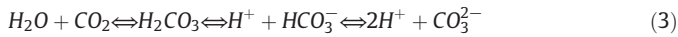


Fig. 12. SEM images of crack lines of ECC and MgO-ECC subjected to the 12th wet-dry cycle using tap water and AMD as immersing liquids.

using Eqs. (5)–(7).



Different wet-dry solution conditions and matrix materials affect the hydraulic conductivity and self-healing results. H^+ released from AMD would dissolve the calcite, magnesite and Mg-rich calcite (Fig. 10), which in turn restrains the resonant frequency (Fig. 4) and induces slightly higher hydraulic conductivity at the same preloading tensile strain (Fig. 7). Adding MgO to ECC produces a considerable amount of hydration compounds such as Ht, hydromagnesite (Figs. 10–13) which induces rapid stabilization of RF values under wet-dry cycles although some of them may have dissolved under the AMD wet-dry condition.

It should be noted that extensive adsorption capability of cutoff wall materials is beneficial to slowing contaminant transportation. Moreover, the effective diffusion coefficient has been identified as one of the most important parameters in predicting contaminant transportation through cutoff walls (Edvardsen, 1999). Therefore, adsorption of real contaminants onto ECC and MgO-ECC as well as diffusive transport of real contaminants across ECC and MgO-ECC vertical cutoff wall materials need to be explored in future studies.

5. Study limitations

ASTM D7100 (2011) specifies the chemical equilibrium, namely consistency in the characteristics of the effluent and influent liquids, during the hydraulic conductivity test. The chemical equilibrium is crucial for investigating long-term containment performance of the hydraulic barriers. When exposed to contaminated liquid (i.e., AMD), the hydraulic conductivity of hydraulic barriers may first increase depending on the contaminant concentration and then tends to a steady-state as the chemical properties of inflow and outflow reach equilibrium (Bohnhoff and Shackelford, 2013; Gulec et al., 2005). When the ECC/MgO-ECC is permeated with AMD, the pH gradually rises due to neutralization of free H^+ in AMD by the OH^- released from the ECC/MgO-ECC. Meanwhile the ion exchange reaction occurs between free H^+ in the AMD and Ca^{2+} and Mg^{2+} released from the ECC and MgO-ECC. Consequently, dissolution of hydration products (i.e., $Ca(OH)_2$, C-S-H and $Mg(OH)_2$) would likely yield a loose structure in ECC or MgO-ECC and then form an easy pathway. Thus, the ion exchange between free H^+ and Ca^{2+}/Mg^{2+} and the dissolution of hydration products may result in an increased hydraulic conductivity depending on test durations. Therefore, establishment of chemical equilibrium in further lab-scale testing program is necessary.

To address the chemical equilibrium, as described in the ASTM D7100 (2011), at least 2 PVF shall be reached, and the solute concentration (i.e., SO_4^{2-} and Fe^{2+}/Fe^{3+} in this study), pH, EC and/or dielectric constant (based on the type of test liquid) of the effluent is expected within $\pm 10\%$ of that for the influent with insignificant increasing or decreasing trend. It should be noted that hydraulic conductivity tests conducted in this study are terminated before the chemical equilibrium is established due to: (1) only 0.80 and 0.76 PVF is achieved at the end of the test; (2) the pH_{out}/pH_{in} values fall beyond $1.0 \pm 10\%$, although the $EC_{in}/$

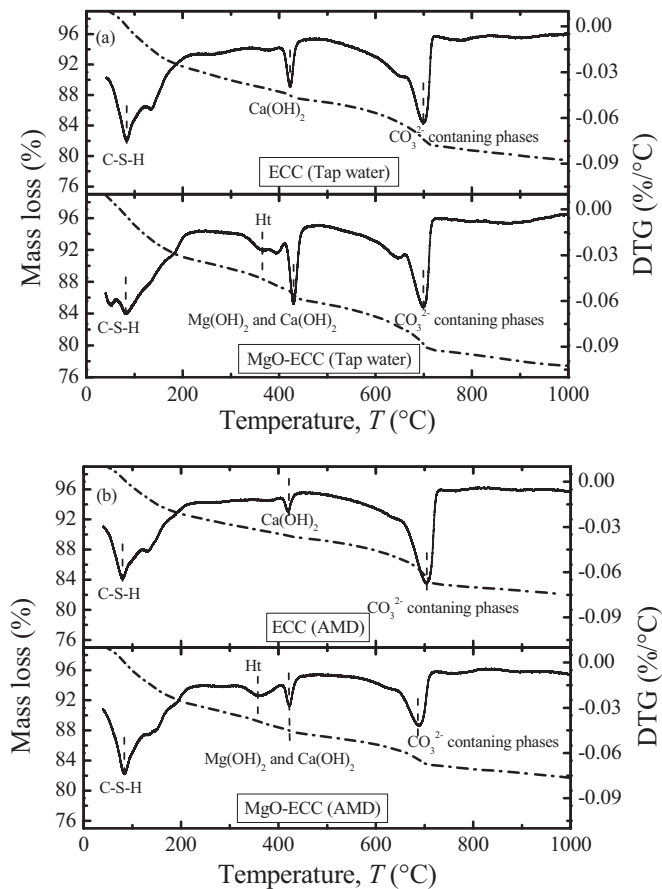


Fig. 13. TGA and DTG analyses conducted on crack lines of ECC and MgO-ECC after subjected to the 12th wet-dry cycle with (a) tap water and (b) AMD.

EC_{out} is within $1.0 \pm 10\%$; and (3) the concentration equilibrium between the effluent and influent liquids for majority ions (i.e., Fe^{2+}/Fe^{3+} and SO_4^{2-}) in AMD is not measured in this study. Moreover, the self-healing could considerably reduce the hydraulic conductivity of cracked specimens during the tested liquid permeation (Lepech and Li, 2009). While at least some self-healing took place during our hydraulic conductivity tests, complete self-healing may require extending the test period. During the hydraulic conductivity tests using tap water or AMD as the permeating liquid, the continued hydration will reduce the porosity of tested specimens. However, only the initial pore volume of each specimen was used to calculate PVF in the uncracked specimens (ECC and MgO-ECC). Thus, the presented hydraulic conductivity results only represent the short-term response of the ECC and MgO-ECC to AMD. Therefore, additional tests including chemical equilibrium conditions and full self-healing recovery are warranted to assess the long-term hydraulic conductivity. Further micro-analysis, i.e., Energy Dispersive Spectrometer (EDS), needs to be conducted to support the SEM and XRD results.

Table 8
Summary of weight loss measured from TGA.

Weight percentage (%)	Tap water		AMD	
	ECC	MgO-ECC	ECC	MgO-ECC
Δm_1	0.51	1.69	0.38	0.91
Δm_2	6.13	5.85	5.82	4.8

6. Conclusions

This study investigated the hydraulic conductivity and self-healing characteristic of typical ECC and ECC incorporating MgO subjected to tap water and acid mining drainage (AMD) solutions via a series of hydraulic conductivity and resonant frequency recovery tests. The effects of AMD exposure and incorporation of MgO on the hydraulic conductivity, resonant frequency and self-healing products of ECC were investigated. Based on the results obtained from this study, the following conclusions can be drawn:

- (1) The addition of MgO to ECC lead to a composite with tighter average crack width ($20 \mu\text{m}$ to $35 \mu\text{m}$) under imposed tensile strain of 0.5–2.0%. This average crack width was 8.7 to 30.3% less than that of ECC with no MgO additive, while the average crack numbers were 7.7% to 28.6% higher than that of ECC under the same strain levels.
- (2) The MgO-ECC exhibited higher integrity than ECC under the same tensile strain of 0%–2.0%, as reflected by the smaller magnitude in RF drops. The type of immersion solution exhibited almost no effect on the RF values for the specimens of ECC and MgO-ECC subjected to the same number of wet-dry cycles. A threshold wet-dry cycle existed for substantial recovery of resonant frequency of cracked ECC and MgO-ECC. This threshold was slightly accelerated by adding MgO but delayed under AMD exposure condition. MgO-ECC specimens displayed higher recovery ratio than ECC specimens irrespective of the type of testing liquid, which was more notable at 2% tensile strain, indicating higher recovery ability of MgO-ECC specimens.
- (3) When permeated with AMD for 39 days, the hydraulic conductivities of un-cracked ECC and MgO-ECC permeated with AMD were 4.51×10^{-12} m/s and 3.12×10^{-12} m/s, respectively. When the tensile strain increased to 2%, the hydraulic conductivities of ECC and MgO-ECC increased to 6.71×10^{-7} m/s and 3.93×10^{-7} m/s, respectively. The hydraulic conductivities of MgO-ECC were 57.84% and 49.8% lower than those of ECC permeated with tap water and AMD, respectively. Upon normalizing by the number of cracks, the hydraulic conductivity of ECC and MgO-ECC specimens dropped one to two magnitudes. When the preloaded tensile strain was less than 1.32%, the normalized hydraulic conductivity of ECC and MgO-ECC permeated with AMD can still meet the commonly accepted limits (10^{-8} m/s).
- (4) SEM and XRD results showed that MgO additive yielded formation of new self-healing products, i.e., hydromagnesite and brucite when exposed to tap water, and Ht when exposed to AMD. The Mg-rich self-healing products in addition to calcite contributed to the improved self-healing performance of MgO-ECC, as confirmed by XRD, FTIR and TGA analyses.

Although additional research is warranted to address the long-term hydraulic conductivity with consideration of not only hydraulic equilibrium condition, but also chemical equilibrium and full self-healing conditions, the findings reported here suggest both ECC and ECC modified with MgO additive can be effective as a construction material for cut-off walls for mine tailing disposal facilities. The relatively low hydraulic conductivity and self-healing functionality of MgO-ECC are conducive to environmental protection against contaminant transport from mining sites.

Declaration of competing interest

The authors declare that there's no financial/personal interest or belief that could affect their objectivity. The authors confirm explicitly that no conflicts of interest exist.

Acknowledgments

The first author is supported by a grant from the Chinese Scholarship Council as a visiting scholar at the University of Michigan. Financial support for this research is partially obtained from the National Key Research and Development Program (Grant Nos. 2018YFC1803100 and 2018YFC1802300), the National Natural Science Foundation of China (Grant No. 41877248), and the Primary Research and Development Plan of Jiangsu Province (Grant No. BE2017715). The authors thank Eastern PA Coalition for Abandoned Mine Reclamation (EPCAMR) for the donated AMD for this study.

References

- ASTM, 2008. Standard Test Method for Fundamental Transverse, Longitudinal, and Torsional Resonant Frequencies of Concrete Specimens, C215. ASTM International, West Conshohocken, PA, USA.
- ASTM, 2011. Standard Test Methods for Hydraulic Conductivity Compatibility Testing of Soils with Aqueous Solutions, D7100. ASTM International, West Conshohocken, PA, USA.
- ASTM, 2012. Standard Specification for Coal Fly Ash and Raw or Calcined Natural Pozzolan for Use in Concrete, C618. ASTM International, West Conshohocken, PA, USA (2012).
- ASTM, 2016a. Standard Specification for Portland Cement, C150/C150M. ASTM International, West Conshohocken, PA, USA (2016).
- ASTM, 2016b. Standard Test Methods for Measurement of Hydraulic Conductivity of Saturated Porous Materials Using a Flexible Wall Permeameter. American Society for Testing and Materials, D5084. ASTM International, West Conshohocken, PA, USA.
- Bohnhoff, G., Shackelford, C., 2013. Hydraulic conductivity of polymerized bentonite-amended backfills. *J. Geotech. Geoenviron. Eng.* 140, 04013028.
- Chau, C.K., Li, Z., 2008. Accelerated reactivity assessment of light burnt magnesium oxide. *J. Am. Ceram. Soc.* 91, 1640–1645.
- Du, Y.J., Jiang, N.J., Liu, S.Y., Jin, F., Singh, D.N., Puppala, A.J., 2014. Engineering properties and microstructural characteristics of cement-stabilized zinc-contaminated kaolin. *Can. Geotech. J.* 51, 289–302.
- Edraki, M., Baumgartl, T., Manlapig, E., Bradshaw, D., Franks, D.M., Moran, C.J., 2014. Designing mine tailings for better environmental, social and economic outcomes: a review of alternative approaches. *J. Clean. Prod.* 84, 411–420.
- Edvardsen, C., 1999. Water permeability and autogenous healing of cracks in concrete. *Dent. Mater. J.* 96, 448–454.
- Espana, J.S., Pamo, E.L., Santofimia, E., Aduvire, O., Reyes, J., Baretino, D., 2005. Acid mine drainage in the Iberian Pyrite Belt (Odiel river watershed, Huelva, SW Spain): geochemistry, mineralogy and environmental implications. *Appl. Geochem.* 20 (7), 1320–1356.
- Fall, M., Célestin, J.C., Han, F.S., 2009. Suitability of bentonite-paste tailings mixtures as engineering barrier material for mine waste containment facilities. *Min. Eng.* 22, 840–848.
- Fernández-Jiménez, A., Palomo, A., 2005. Composition and microstructure of alkali activated fly ash binder: effect of the activator. *Cem. Concr. Res.* 35, 1984–1992.
- Gulec, S., Benson, C., Edil, T., 2005. Effect of acidic mine drainage on the mechanical and hydraulic properties of three geosynthetics. *J. Geotech. Geoenviron. Eng.* 131, 937–950.
- Haha, M.B., Lothenbach, B., Le Saout, G.L., Winnefeld, F., 2011. Influence of slag chemistry on the hydration of alkali-activated blast-furnace slag—part I: effect of MgO. *Cem. Concr. Res.* 41, 955–963.
- Huang, X., Ranade, R., Li, V.C., 2012b. Feasibility study of developing green ECC using iron ore tailings powder as cement replacement. *J. Mater. Civ. Eng.* 25, 923–931.
- Huang, X.Y., Ni, W., Cui, W.H., Wang, Z.J., Zhu, L.P., 2012a. Preparation of autoclaved aerated concrete using copper tailings and blast furnace slag. *Constr. Build. Mater.* 27, 1–5.
- Jin, F., Al-Tabbaa, A., 2014a. Evaluation of novel reactive MgO activated slag binder for the immobilisation of lead and zinc. *Chemosphere* 117 (2014), 285–294.
- Jin, F., Al-Tabbaa, A., 2014b. Characterization of different commercial reactive magnesia. *Adv. Cem. Res.* 26 (2014), 101–113.
- Joshi, K., Kechavarzi, C., Sutherland, K., Ng, M.Y.A., Soga, K., Tedd, P., 2009. Laboratory and in situ tests for long-term hydraulic conductivity of a cement-bentonite cutoff wall. *J. Geotech. Geoenviron. Eng.* 136 (2009), 562–572.
- JSCE, 2008. Recommendations for Design and Construction of High Performance Fiber Reinforced Cement Composites With Multiple Fine Cracks. HPRCC, Tokyo.
- Kanellopoulos, A., Qureshi, T.S., Al-Tabbaa, A., 2015. Glass encapsulated minerals for self-healing in cement based composites. *Constr. Build. Mater.* 98.
- Kashir, M., Yanful, E.K., 2000. Compatibility of slurry wall backfill soils with acid mine drainage. *Adv. Environ. Res.* 4, 251–268.
- Lepech, M.D., Li, V.C., 2009. Water permeability of engineered cementitious composites. *Cem. Concr. Compos.* 31, 744–753.
- Li, V.C., 2019. Engineered Cementitious Composites (ECC): Bendable Concrete for Sustainable and Resilient Infrastructure. Springer Press.
- Liu, H., Zhang, Q., Gu, C., Su, H., Li, V.C., 2016. Influence of micro-cracking on the permeability of engineered cementitious composites. *Cem. Concr. Compos.* 72, 104–113.
- Liu, H., Zhang, Q., Gu, C., Su, H., Li, V., 2017. Influence of microcrack self-healing behavior on the permeability of engineered cementitious composites. *Cem. Concr. Compos.* 82, 14–22.
- Lobbestael, A.J., 2014. An Investigation of the Seismic Response of Earthen Levees With Cutoff Walls With a Focus on the Development of a High Performance Cutoff Wall Material. PhD thesis. The University of Michigan, USA.
- Özbay, E., Karahan, O., Lachemi, M., Hossain, K.M., Atis, C.D., 2013. Dual effectiveness of freezing–thawing and sulfate attack on high-volume slag-incorporated ECC. *Compos. Part B* 45, 1384–1390.
- Qureshi, T.S., Al-Tabbaa, A., 2016. Self-healing of drying shrinkage cracks in cement-based materials incorporating reactive MgO. *Smart Mater. Struct.* 25, 084004.
- Qureshi, T.S., Kanellopoulos, A., Al-Tabbaa, A., 2016. Encapsulation of expansive powder minerals within a concentric glass capsule system for self-healing concrete. *Constr. Build. Mater.* 121, 629–643.
- Qureshi, T.S., Kanellopoulos, A., Al-Tabbaa, A., 2018. Autogenous self-healing of cement with expansive minerals-I: impact in early age crack healing. *Constr. Build. Mater.* 192, 768–784.
- Qureshi, T.S., Kanellopoulos, A., Al-Tabbaa, A., 2019. Autogenous self-healing of cement with expansive minerals-II: impact of age and the role of optimised expansive minerals in healing performance. *Constr. Build. Mater.* 194, 266–275.
- Ruffing, D.G., Evans, J.C., 2014. Case study: construction and in situ hydraulic conductivity evaluation of a deep soil-cement-bentonite cutoff wall. *Geo-Congress 2014: Geo-Characterization and Modeling for Sustainability*, pp. 1836–1848.
- Scrivener, K., Snellings, R., Lothenbach, B., 2016. A Practical Guide to Microstructural Analysis of Cementitious Materials. CRC Press.
- Shen, S., Wu, Y., Misra, A., 2017. Calculation of head difference at two sides of a cut-off barrier during excavation dewatering. *Comput. Geotech.* 91 (2017), 192–202.
- Sherir, M.A., Hossain, K.M., Lachemi, M., 2016. Self-healing and expansion characteristics of cementitious composites with high volume fly ash and MgO-type expansive agent. *Constr. Build. Mater.* 127, 80–92.
- Sherir, M.A., Hossain, K.M., Lachemi, M., 2017. The influence of MgO-type expansive agent incorporated in self-healing system of engineered cementitious composites. *Constr. Build. Mater.* 149, 164–185.
- Shettima, A.U., Hussin, M.W., Ahmad, Y., Mirza, J., 2016. Evaluation of iron ore tailings as replacement for fine aggregate in concrete. *Constr. Build. Mater.* 120, 72–79.
- Song, S., Jennings, H.M., 1999. Pore solution chemistry of alkali-activated ground granulated blast-furnace slag. *Cem. Concr. Res.* 29, 159–170.
- USEPA, 1994. U.S. Environmental Protection Agency Technical Report: Design and Evaluation of Tailings Dams. Author, Washington, DC.
- Valente, T.M., Gomes, C.L., 2009. Occurrence, properties and pollution potential of environmental minerals in acid mine drainage. *Sci. Total Environ.* 407, 1135–1152.
- Van Zijl, G.P., Slowik, V., 2017. A Framework for Durability Design With Strain-hardening Cement-based Composites (SHCC): State-of-the-art Report of the RILEM Technical Committee 240-FDS. Springer.
- Wang, K., Jansen, D.C., Shah, S.P., Karr, A.F., 1997. Permeability study of cracked concrete. *Cem. Concr. Res.* 27, 381–393.
- Wang, S., Scrivener, K.L., 1995. Hydration products of alkali activated slag cement. *Cem. Concr. Res.* 25, 561–571.
- Wu, H.L., Jin, F., Bo, Y.L., Du, Y.J., Zheng, J.X., 2018a. Leaching and microstructural properties of lead contaminated kaolin stabilized by GGBS-MgO in semi-dynamic leaching tests. *Constr. Build. Mater.* 172, 626–634.
- Wu, H.L., Zhang, D., Ellis, B.R., Li, V.C., 2018b. Development of reactive MgO-based engineered cementitious composite (ECC) through accelerated carbonation curing. *Constr. Build. Mater.* 191, 23–31.
- Wu, H.L., Jin, F., Ni, J., Du, Y.J., 2019a. Engineering properties of vertical cutoff walls consisting of reactive magnesia-activated slag and bentonite: workability, strength, and hydraulic conductivity. *J. Mater. Civ. Eng.* 31 (11), 04019263.
- Wu, H.L., Yu, J., Zhang, D., Zheng, J.X., Li, V.C., 2019b. Effect of morphological parameters of natural sand on mechanical properties of engineered cementitious composites. *Cem. Concr. Compos.* 100, 108–119.
- Wu, H.L., Jin, F., Du, Y.J., 2019c. Influence of wet-dry cycles on vertical cutoff walls made of reactive magnesia-slag-bentonite-soil mixtures. *J. Zhejiang Univ., Sci., A* 20 (12), 948–960.
- Wu, M., Johansson, B., Geiker, M., 2012. A review: self-healing in cementitious materials and engineered cementitious composite as a self-healing material. *Constr. Build. Mater.* 28, 571–583.
- Xu, S., Cai, X., 2010. Experimental studies on permeability and carbonation properties of ultra-high toughness cementitious composites. *Acta Materialia Composita Sinica* 3, 028.
- Yang, Y., Lepech, M.D., Yang, E., Yang, E., Li, V.C., 2009. Autogenous healing of engineered cementitious composites under wet–dry cycles. *Cem. Concr. Res.* 39, 382–390.
- Yang, Y., Yang, E., Li, V.C., 2011. Autogenous healing of engineered cementitious composites at early age. *Cem. Concr. Res.* 41, 176–183.
- Yang, Y.L., Reddy, K.R., Du, Y.J., Fan, R.D., 2018. SHMP amended calcium bentonite for slurry trench cutoff walls: workability and microstructure characteristics. *Can. Geotech. J.* 144 (6), 120–127.
- Yu, J., Li, H., Leung, C.K.Y., Lin, X., Lam, J.Y.K., Sham, I.M.L., Shih, K., 2017. Matrix design for waterproof engineered cementitious composites (ECCs). *Constr. Build. Mater.* 139 (2017), 438–446.
- Yu, J., Yao, J., Lin, X., Li, H., Lam, J.Y.K., Leung, C.K.Y., Sham, I.M.L., Shih, K., 2018. Tensile performance of sustainable Strain-Hardening Cementitious Composites with hybrid PVA and recycled PET fibers. *Cem. Concr. Res.* 107, 110–123. <https://doi.org/10.1016/j.cemconres.2018.02.013>.
- Zhang, Z., Zhang, Q., 2017. Self-healing ability of engineered cementitious composites (ECC) under different exposure environments. *Constr. Build. Mater.* 156, 142–151.
- Zhao, Z., 2012. Transport Properties of Pseudo Ductile Cementitious Composites. MPhil thesis. Hong Kong University of Science and Technology, Hong Kong SAR, China.